Artificial control of ZnO nanodots by ion-beam nanopatterning

Sang-Woo Kim
Department of Metallurgical Engineering, Kumoh National Institute of Technology, 1 Yangho-dong, Gumi, Gyeongbuk 730-701, Republic of Korea

Masaya Ueda, Mitsuru Funato, and Shigeo Fujita
Department of Electronic Science and Engineering, Kyoto University, Katsura, Nishikyo-ku, Kyoto 615-8510, Japan

Shizuo Fujita[a)]
International Innovation Center and Advanced Research Institute for Nanoscale Science and Technology, Kyoto University, Katsura, Nishikyo-ku, Kyoto 615-8510, Japan

(Received 13 September 2004; accepted 7 March 2005; published online 5 May 2005)

The use of focused ion-beam (FIB) nanopatterning for manipulating self-assembled ZnO nanodots is described. Highly aligned ZnO-nanodot arrays with various periodicities (e.g., 750, 190, and 100 nm) on FIB-nanopatterned SiO_2/Si substrates were prepared by metal-organic chemical-vapor deposition (MOCVD). The artificially assembled ZnO nanodots had an amorphous structure. Ga atoms incorporated into the surface areas of FIB-patterned nanoholes during FIB engraving were found to play an important role in the artificial control of ZnO, resulting in the production of ZnO nanodots on the FIB-nanopatterned areas. The nanodots evolved into single-crystalline dot clusters and rods with increasing MOCVD-growth time. In addition, microphotoluminescence measurements showed that the ZnO-nanodot arrays have low-dimensional quantum characteristics. © *2005 American Institute of Physics*. [DOI: 10.1063/1.1898446]

I. INTRODUCTION

Self-assembled ZnO nanostructures such as nanodots,[1] nanowires,[2] nanorods,[3] nanobelts,[4] and nanotubes[5] have attracted a great deal of attention for use in various applications including nanoscale optical devices, field emitters, nanoscale circuits, and nanosensors. In addition, a special interest exists in the optoelectronic research community, as the result of the promising optical properties of ZnO (e.g., a large exciton binding energy of 60 meV and biexciton binding energy of 15 meV).[6] However, in spite of a number of reports on the fabrication of self-assembled ZnO nanostructures, one of the major obstacles to achieving ZnO-based nanostructure-building blocks is the ability to control ZnO nanostructures with a desired size and forming position in the synthesis process. In this regard, some groups have attempted to manipulate the position and size of ZnO nanostructures.[7,8] However, only a few systematic reports have appeared with detailed information relative to controlling the dimension and chirality of nanostructures by synthesis methods. Recently, our group reported on the control of the position and size of ZnO nanodots using metal-organic chemical-vapor deposition (MOCVD) in conjunction with nanopatterning by focused ion beam (FIB). However, the mechanism of formation of artificially controlled ZnO nanodots is currently unclear. Information on the mechanism for the selective formation of ZnO nanodots on FIB-engraved nanohole arrays would attract a great deal of attention in other interdisciplinary fields of nanotechnologies as well as the ZnO-related research community. We report herein on the preparation of position- and size-manipulated ZnO nanodots, in which a systematic study of the formation mechanism and the characterization of ZnO nanodots was carried out.

II. EXPERIMENT

In order to fabricate ZnO nanodots with a controlled morphology and dimension, we introduced a combination of a "bottom-up"–"top-down" approach based on MOCVD and FIB (SEIKO SMI-2050)-functionalized substrates.[7,9] The nanopatterned substrates for the growth of manipulated ZnO nanodots were prepared by the FIB nanoengraving of SiO_2/Si substrates. Typical flow rates of source materials for the MOCVD growth of ZnO, diethylzinc (DEZn) and N_2O, were 1 and 7000 μmol/min, respectively, where the pressure in the MOCVD reactor was maintained at 200 Torr. The substrate temperatures were in the range of 500–700 °C so as to study the effect of temperature on the selective growth of ZnO nanodots in nanohole arrays on the substrates prepared by FIB.

The crystal structure of the artificially controlled ZnO nanodots on SiO_2/Si substrates was analyzed by transmission electron microscopy (TEM, HITACHI H-9000NAR, 300-kV accelerating voltage). The formation of not only nanodots but also a combination of clusters and rods were confirmed by atomic force microscopy (AFM, SEIKO SPA-400) and field-emission scanning electron microscopy (FE-SEM, JEOL JSM-7400). The composition of the selectively grown ZnO nanodots in nanopatterned arrays was determined by microenergy-dispersive x-ray spectroscopy (μ-EDX) linked with a TEM instrument (HITACHI HF-2000, 200-kV accelerating voltage), in addition with SEM-EDX (attached to JEOL JSM-6500F) measurements. The optical properties of the ZnO nanodots were characterized by cathodolumines-

[a)]Electronic mail: fujita@iic.kyoto-u.ac.jp

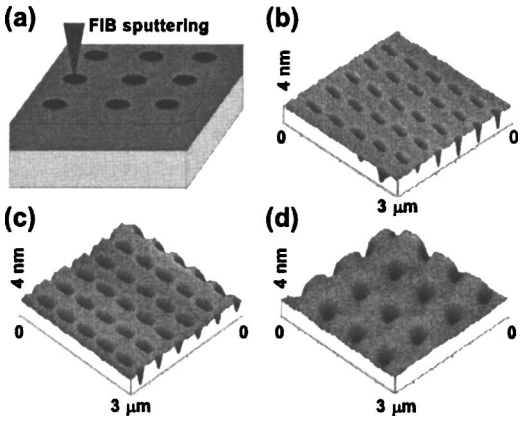

FIG. 1. Schematic image of the FIB sputtering of a SiO_2/Si substrate with 30-keV Ga^+ ions. AFM images (b, c, and d) of 2D nanopattern arrays engraved by FIB are shown here. Nanopatterns were produced under a programming command of fabricating a constant depth of 6 nm, by varying the beam diameter (beam current) of 13 (b, 1 pA), 23 (c, 48 pA), and 100 nm (d, 1.3 nA).

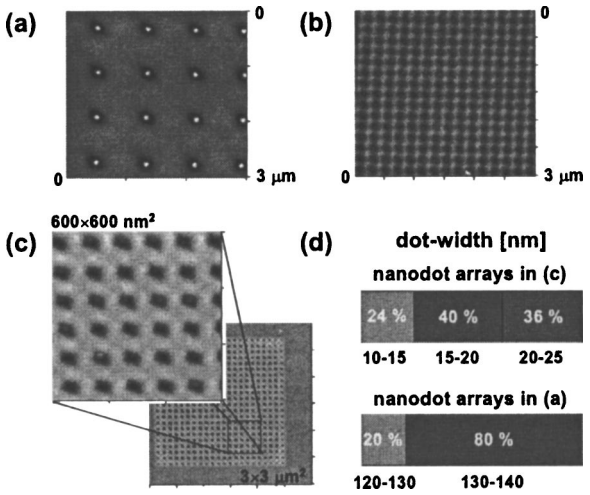

FIG. 2. Plan-view AFM images of 2D ZnO-nanodot arrays with different periodicities. (a) 750, (b) 190, and (c) 100 nm. Distribution of the nanodots shown in (a) and (c) in their widths is presented at (d).

cence (CL) measurements at room temperature (RT) with a system equipped with a FE-SEM instrument (JEOL JSM-6500F) and microphotoluminescence (μ-PL) measurements performed by fluorescent microscopy (NIKON Y-FL) using the 325-nm line of a He–Cd laser (20 mW) as the excitation source.

III. RESULTS AND DISCUSSION

A. FIB Nanopatterning

In order to fabricate spatially regular arrays of nanostructures, appropriately shaped patterns were introduced into the substrate followed by MOCVD growth of the ZnO into the patterns. Recently, nontraditional nanofabrication technologies such as FIB lithography,[10] near-field optical lithography,[11] and contact printing techniques[12] have been actively developed. Of these, FIB, utilizing a direct sputtering process, has many unique advantages over other similar types of techniques for nanofabrication: (1) maskless rapid prototyping, (2) its sub- 10-nm spot size enables the patterning of diverse nanostructures at very high resolution, and (3) allowing the production of high-resolution patterns without refocusing or changing the sample height.

In this work, SiO_2(50 nm)/Si substrates were patterned in a FIB chamber to create two-dimensional (2D) arrays of nanoholes. A Ga^+ liquid-metal ion source, in which the beam energy was fixed at 30 keV, with an ion dose of 1×10^{16} cm^{-2} was used. The ion-beam size is a function of the beam current as programmed FIB properties. The beam currents were varied from 1 pA to 1.3 nA in order to control the dimensions of the nanoholes engraved by FIB. Details concerning the patterning modes of the FIB system for high-speed nanoengraving over a wide area have been described elsewhere.[13]

Numerous sputtering conditions were examined to realize the desired nanohole profiles. Figure 1 shows AFM images of 2D nanohole arrays patterned under a programming command of fabricating a 6-nm constant depth with varying the beam sizes of 13 (a), 23 (b), and 100 nm (c). The beam diameter directly corresponded to that of the nanohole at the top surface. On the other hand, the sputtering time required for achieving the same sputtering depth among the three patterns was different. A large beam size leads to a short processing time at the expense of increase in the individual holes. Using optimized FIB-sputtering conditions we succeeded in forming 2D nanohole arrays with various periodicities (e.g., 750, 190, and 100 nm) over a wide area.

B. Selective formation of ZnO nanodots

Figure 2 shows AFM images of highly aligned 2D ZnO-nanodot arrays formed in FIB-engraved nanoholes (patterning depth: 6 nm) with different periodicities at a MOCVD-growth temperature of 700 °C for 40 s. From the AFM study shown in Fig. 2 the average heights [9 (a), 5 (b), and 4 nm (c)] and average widths [130 (a), 40 (b), and 25 nm (c)] of individual nanodots selectively grown on each nanohole array are closely related to the dimensions of the nanoholes, indicating that a nanohole with a larger dimension accommodates a larger ZnO nanodot. The perfect one-by-one accommodation of a ZnO nanodot in a nanohole was realized in the samples of 2D nanohole arrays with 750- and 190-nm periodicities, while the packing percentage of ZnO nanodots in the nanoholes with a 100-nm periodicity was about 64% in addition to a large distribution in their widths [Fig. 2(d)]. The low packing percentage is due to the relatively high growth temperature of 700 °C, resulting in an increase in the atomic desorption of reacting species from the surface of the pattern. Very recently, the selective formation of ZnO nanodots with a packing percentage higher than 75% into the nanoholes shown in Fig. 2(c) was realized, using more optimized growth conditions, which will be reported elsewhere.

In order to study the characteristics of the selective growth and evolution of ZnO nanodots as a function of MOCVD-growth time, we varied the growth time from 40 s to 600 and 900 s. Figure 3 shows that, when the MOCVD-growth time is increased, the nanodots are converted to clusters [600 s, Fig. 3(b)] and rods [900 s, Figs. 3(c) and 3(d)] on FIB-nanopatterned holes. An increase in the average dot

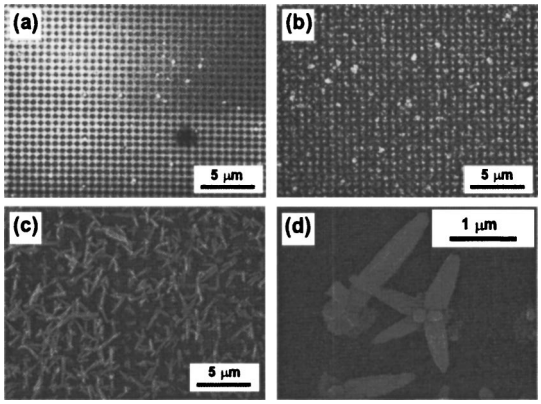

FIG. 3. FE-SEM images of selectively grown ZnO nanodots (a), clusters (b), and rods (c). The image shown in (d) is a magnified image of (c). The growth time for the formation of nanodots (a), clusters (b), and rods (c) is 40, 600, and 900 s, respectively. Although some rods fall down on the substrate surface, all are selectively well grown on the 2D nanohole arrays.

width was linear with respect to growth time, while the average dot height was less sensitive to growth time. When sufficient growth time (over 600 s) was used, the average volume (Fig. 4) of the grown ZnO nanostructures increased superlinearly with the increment of growth time, resulting in the formation of rod structures with random growth directions. The superlinear increase in volume can be attributed to a dramatic increase in the height of the ZnO nanostructures, leading to the dots being converted to rods with high aspect ratios. This indicates that FIB-patterned nanoholes act as seeds for the growth of ZnO nanodots, clusters, and rods as a function of growth time. It should be noted, however, that, contrary to the one-by-one accommodation of nanodots in nanoholes, 3–6 clusters (large-sized dots) and rods are accommodated in a nanohole, as shown in Figs. 3(b)–3(d). The mechanism for the selective formation of nanodots, clusters, and rods on nanopatterned holes will be described in detail in Sec. III C.

Figure 5 shows a plan-view SEM image of ZnO clusters selectively grown in nanoholes for 600 s and a RT-CL image taken at a wavelength of 374 nm in addition to the measured CL spectrum. The strong emission band at 374 nm in the scanned spectrum taken with the CL system indicates that the origin of the emission can be attributed to the near band-edge emission of ZnO considering its band gap of 3.37 eV. The resulting monochromatic CL image taken using the 374-nm

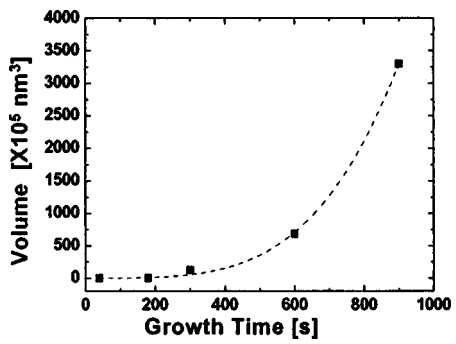

FIG. 4. Volume evolution of grown ZnO (from nanodots to clusters and rods) as a function of MOCVD-growth time.

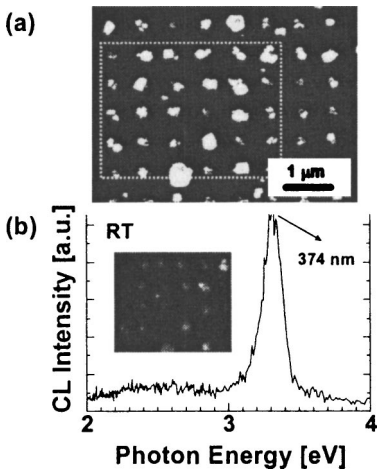

FIG. 5. (a) FE-SEM image of well-aligned ZnO clusters grown for 600 s. (b) CL spectrum of the FE-SEM image (a) measured at RT. The inset shows RT-CL image taken at the wavelength of 374 nm from the area designated as a dotted square in the FE-SEM image (a).

luminescence peak represents an excellent map of the luminescence from the area designated by a box in the SEM image, thus permitting the formation of stoichiometric ZnO clusters to be visualized.

C. Formation mechanism of ZnO nanodots on FIB-patterned nanoholes

The bottom and sidewall of the sputtered nanohole are also SiO_2 with amorphous structural properties because the thickness of the thermally grown SiO_2 layer on Si substrates is 50 nm and the depth sputtered by FIB is 6 nm in all samples used in this work. Thus, it can be concluded that a change in the surface structure, such as the generation of surface atomic steps and kinks by energetic Ga^+ ions, is not related to the selective formation of ZnO nanodots on the FIB-sputtered SiO_2 areas.

Our previous study suggested the possibility that Ga atoms are incorporated into patterns during the FIB engraving.[9] In order to investigate the effect of Ga atoms incorporated into patterns from the ion beam for nucleation of ZnO, we carried out the growth of ZnO using a substrate (substrate 1) which is different from the previous one (substrate 2) shown in Fig. 1. A schematic image for comparison between the two types of substrates is shown in Fig. 6 and surface AFM images for substrate 1 observed at each step are shown in Fig. 7. For substrate 1, after preparing FIB-engraved 2D nanohole arrays on a Si substrate [Fig. 7(a)], we carried out thermal oxidation of it in a furnace at 1000 °C for 10 min in an oxygen atmosphere to allow the incorporated Ga atoms in the patterned holes to form Ga_xO_{1-x}. In order to exclude the effect of Ga on ZnO nucleation, the thermally formed Ga_xO_{1-x} was lifted off, and the thermally grown SiO_2 layer eliminated using a diluted HF solution [Fig. 7(b)]. SEM-EDX measurements confirmed that Ga atoms that were incorporated during the FIB nanopatterning were completely eliminated by the lift-off process. The reoxidation of the HF-treated substrate with an oxide thickness of 50 nm (1000 °C for 40 min) was then carried out to achieve a SiO_2/Si substrate with 2D nanohole arrays, with a 750-nm periodicity

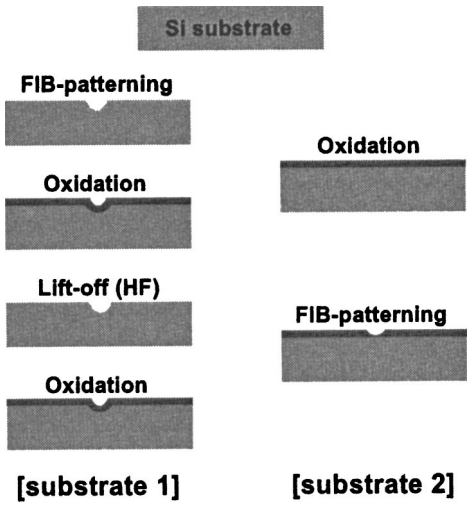

FIG. 6. Schematic image for comparison between two kinds of substrates (substrates 1 and 2) patterned by FIB for ZnO growth to clarify mechanism on the selective formation of ZnO nanodots on 2D nanoholes.

[Fig. 7(c), the same as the substrate shown in Fig. 2(a)]. After the reoxidized substrate was transferred to the MOCVD reactor, Zn and O species were supplied for ZnO growth. The feature of ZnO grown under the same growth conditions, as were used for the ZnO nanodots on the reoxidized substrate presented in Fig. 2(a), is shown in Fig. 7(d). A number of smaller nanodots compared with those in Fig. 2(a) [also shown at Fig. 7(f)] are formed into nanoholes as well as on the planar SiO_2 surface between the nanoholes [Fig. 7(e)], indicating that the nanoholes did not act as artificial traps for migrating Zn and O adatoms and manipulated nucleation seeds for ZnO any longer. The random formation of these nanodots in their positions irrespective of the existence of nanoholes is similar to that of self-assembled ZnO nanodots on planar SiO_2/Si substrates, as reported in our previous studies.[1,14]

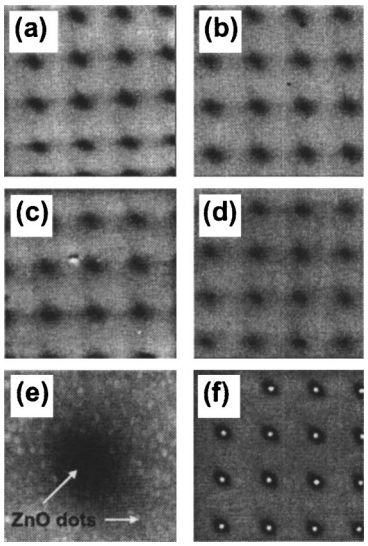

FIG. 7. Plan-view AFM images [the image scale of (a)–(d) and (f) is 3 $\times 3$ μm^2 and that of (e) is 600×600 nm^2] of (a) FIB-engraved 2D nanohole arrays on a Si substrate, (b) chemically (a dilute HF solution) treated substrate after a thermal oxidation at 1000 °C for 10 min, (c) reoxidation of the HF-treated substrate at 1000 °C for 40 min, (d) randomly grown ZnO nanodots on (c), (e) a nearby area of a single nanohole in the sample (d), and (f) well-aligned ZnO nanodots selectively grown on the substrate (a), which is also shown in Fig. 2(a).

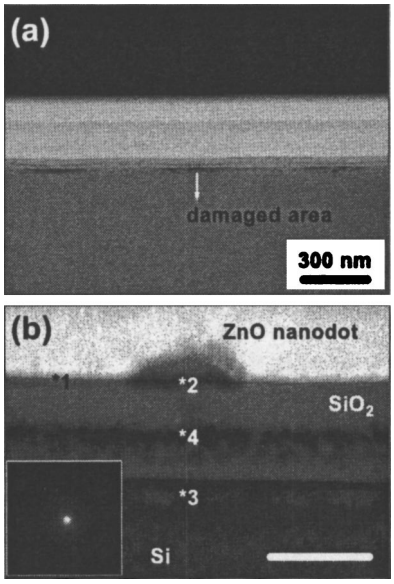

FIG. 8. Side-view bright-field TEM images of selectively grown ZnO nanodots on nanoholes shown in Fig. 3(a). (a) TEM image of nanodots grown on three arrayed nanoholes. (b) TEM image of a ZnO nanodot on a nanohole. The inset of (b) is selective area TED pattern of the ZnO nanodot with an amorphous-crystalline structure grown on the nanohole. The scale bar in the image (b) indicates 50 nm.

Figure 8 shows cross-sectional bright-field TEM images of selectively grown ZnO nanodots [the sample shown in the Fig. 3(a)] on the nanoholes. No significant crystalline lattices were observed in the ZnO dot area, indicating that the structure of the ZnO grown on the nanopattern is amorphous. The amorphous structure of the ZnO nanodot was also confirmed from the selective area transmission electron-diffraction (TED) pattern shown in the inset of Fig. 8(b). In order to clarify the mechanism for the selective formation of ZnO nanodots on nanoholes, we carried out μ-EDX measurements at points corresponding to the cross sections of the sample. The μ-EDX spectra were recorded at different positions of the nanodot and the substrate area for composition analyses. The spectrum shown in Fig. 9(a) was obtained

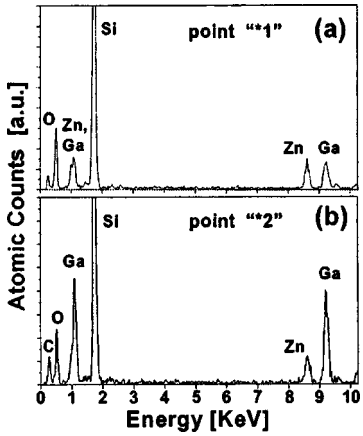

FIG. 9. (a) and (b) show μ-EDX spectra recorded at the points marked as $^{*}1$ and $^{*}2$ in Fig. 8(b), respectively.

from the planar unpatterned SiO_2 surface between nanoholes [marked as "*1" in Fig. 8(b)], which clearly shows the characteristic peaks corresponding to Zn and Ga as well as Si and O. The intensity of the Zn- and Ga-related peaks is comparable, but is quite weak. On the other hand, the intensity of the Ga peak is much stronger than that of the Zn peak in the spectrum shown in Fig. 9(b), which was measured at the interface area [marked as "*2" in Fig. 8(b)] between the dot and the surface of the nanohole. This result is reasonable, considering the Gaussian profile of the ion beam.[15] The incorporation of Ga atoms in area '*1' might be due to ion-beam broadening caused by the surface charging of the insulating SiO_2 surface. The dark area [denoted as "*3" in Fig. 8(b)] on the Si surface below the thermally grown SiO_2 layer is a damage-induced area, produced by energetic Ga^+ ions during the FIB nanoengraving. Ga and Cu atoms as well as major Si and O atoms were detected from the clusters in the SiO_2. The formation of clusters ["*4" area in Fig. 8(b)] composed of Ga and Cu atoms might be due to the incorporation of Ga atoms during FIB patterning and Cu diffusion from the Si to the SiO_2 layer during the MOCVD-growth temperature at 700 °C. Our simulation showed that Ga^+ ions that are accelerated by 30 keV can penetrate to depths of more than 60 nm and that the maximum Ga concentration is at around 30 nm from the SiO_2 surface. From these findings and the SiO_2 thickness of 50 nm, it can be concluded that the damaged area (*3) is induced by Ga^+ ions and that the clusters consisting of Ga and Cu (*4) are formed at the depth where the Ga concentration is at a maximum.

From the above discussion, in conjunction with Figs. 6–9, we propose the mechanism for the evolution of ZnO nanodots to clusters and rods on FIB-patterned nanoholes as a function of MOCVD-growth time. The schematic images are presented in Fig. 10. A number of Ga atoms are incorporated into the SiO_2 layer during FIB nanoengraving, even though Si and O atoms are simultaneously etched out by energetic Ga^+ ions. The Ga atoms that are incorporated in the patterned nanohole were molten before reaching the ZnO-growth temperature of 700 °C in this study because the melting point of Ga is about 30 °C. At the early stage of MOCVD growth, Zn atoms that decompose from the DEZn are absorbed into the molten Ga atoms, which are mainly anchored on the nanoholes, forming a solid solution of Zn–Ga. Once the Zn–Ga solid solution is supersaturated, the continuous supply of Zn and O species results in the formation of amorphous ZnO nanodots on the supersaturated surface[16] of the Ga-incorporated area into the nanohole. Therefore, we conclude that the amorphous ZnO nanodot with a Zn-abundant phase, as confirmed by the μ-EDX measurements, directly grew out from the supersaturated surface. As mentioned above, Zn atoms were also detected on the planar unpatterned SiO_2 surface between the nanoholes. However, no ZnO-related emission by selective excitation of the surface area, denoted as '*1', was observed in the RT-CL measurements, while a ZnO band-edge emission was clearly observed from a single dot on a nanohole.[13] This indicates that only a small number of Zn and O adatoms were incorporated into area '*1'. However, spontaneous dot nucleation followed by growth and coarsening only occurs in area '*2' of the nanohole. From the μ-EDX spectra in Fig. 9, the quantity of incorporated Ga atoms in the '*1' area is clearly much smaller than that in area '*2' in the nanohole, indicating that sufficient numbers of Ga atoms to act as a catalyst are required for effective ZnO nucleation.

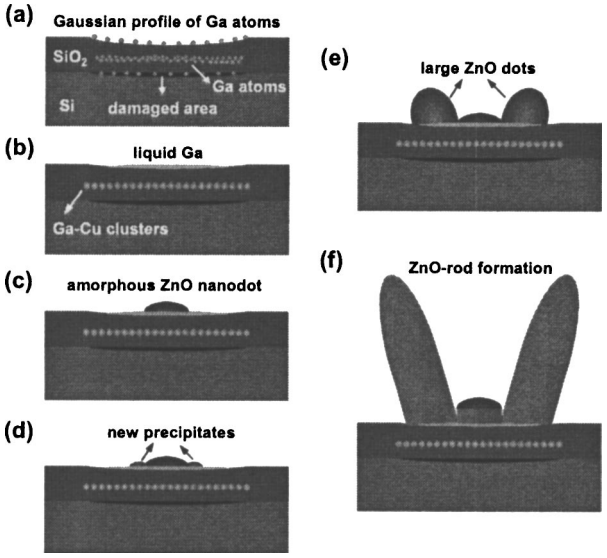

FIG. 10. Schematic images showing the evolution of ZnO nanodots into clusters and rods in nanoholes, as a function of MOCVD-growth time. (a) Ga atoms are incorporated with a Gaussian profile into the patterned SiO_2 layer. The incorporation of Ga atoms is propagated up to the damaged areas (dark areas) on the Si surface below the thermally grown SiO_2 layer. Simulation results showed that the maximum propagation depth of Ga atoms through SiO_2 is about 60 nm in the patterning condition of this study. (b) The incorporated Ga atoms melt before the main MOCVD-growth temperature at 700 °C. Clusters into the SiO_2 layer are composed of Ga and Cu atoms. (c) Formation of an amorphous ZnO nanodot on the supersaturated surface of the Ga-incorporated area into a nanohole. (d) ZnO precipitates with a single-crystalline structure are formed on the close vicinity of the amorphous ZnO nanodot due to catalyst-poisoning effects. (e) The ZnO precipitates rather than the amorphous ZnO nanodots are enlarged by successive supply of Zn and O species, resulting in large ZnO dots. (f) The large ZnO dots lead to the formation of ZnO rod structures through sufficient growth.

The formation of amorphous ZnO nanodots may cause a catalyst-poisoning effect,[17] inactivating the interface and cutting off the Zn and O supply to the supersaturated surface. Some large dots, as shown in Fig. 3(a), are also formed irregularly on the substrate in addition to uniform small nanodots. From a careful observation of the SEM image in Fig. 3(a), the large dots are formed not on the central area of the nanohole surface but in the vicinity of the nanoholes. The TEM observation of a large dot [Fig. 11(b)] also clearly shows that a large dot with a single-crystalline structure is formed in proximity to an amorphous ZnO dot grown on the central area of a nanohole surface. The catalyst-poisoning effect causes the Zn and O supply beneath the amorphous ZnO to be cut off. Thus, the source supply is concentrated around the amorphous ZnO nanodot, and new ZnO precipitates with a single-crystalline structure are formed in close proximity to the amorphous ZnO nanodot [Fig. 11(a)]. The absorption and diffusion of Zn and O can be enhanced at the surfaces of the ZnO precipitates during growth.[18] Further successive supply of Zn and O species results in the coarsening of the ZnO precipitates rather than amorphous ZnO nanodots.

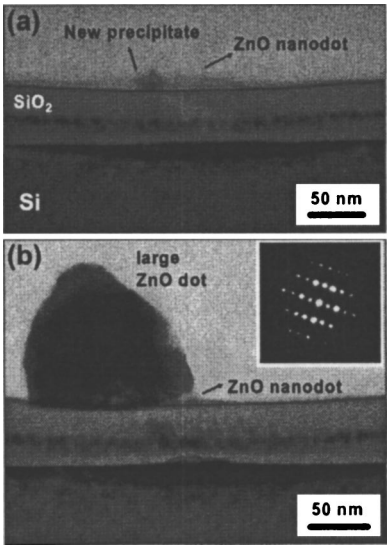

FIG. 11. Cross-sectional bright-field TEM images as supporting evidence for the process shown in Figs. 10(d) and 10(e). (a) Formation of a ZnO precipitate on the close vicinity of the amorphous ZnO nanodot. (b) A large ZnO dot is formed on the close vicinity of the amorphous ZnO nanodot grown on the center of a nanohole surface because the absorption and diffusion of Zn and O are enhanced at the surfaces of the ZnO precipitate during growth. The inset is selective area TED-pattern image of the large ZnO dot, which clearly shows that the large dot has a single-crystalline structure.

Although the number of the ZnO precipitates [Fig. 11(a)] and large dots [Fig. 11(b)] is small, these structures coexist with uniform amorphous ZnO nanodots [Fig. 8(b)] on the same sample. The cause of this is unclear at present, but might be due to different critical evolution times that depend on the degree of the catalyst-poisoning effect. Ga atoms incorporated by FIB result in the selective growth of ZnO. At the same time, however, Ga atoms prevent ZnO nuclei from crystallizing, which results in the formation of amorphous ZnO nanodots that serve as the origin of the catalyst-poisoning effect. We conclude that the number of Ga atoms varies from position to position due to local ion-beam fluctuations during the FIB patterning, causing changes in the degree of the catalyst-poisoning effect. Figure 12 clearly shows that self-assembled ZnO nanodots on planar unpatterned SiO_2/Si substrates have a single-crystalline structure with hexagonal atomic arrays without any types of defects in spite of the amorphous nature of SiO_2.[1,19] From the experiment results, it could be confirmed that the formation of artificially controlled ZnO nanodots with an amorphous structure is due to the Ga atoms incorporated during the FIB engraving process.

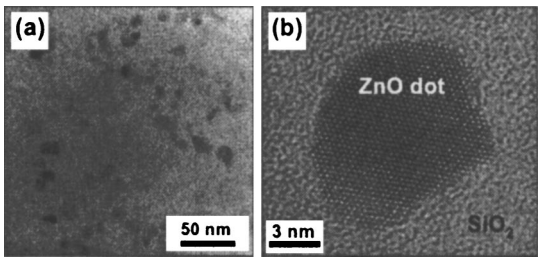

FIG. 12. (a) Plan-view TEM image of self-assembled ZnO nanodots on a SiO_2/Si substrate (dot density: 1.1×10^{11} cm^{-2}) by MOCVD. The widths of the individual nanodots range from 5 to 15 nm (an average height of the nanodots is about 7 nm). (b) High-resolution TEM image of a self-assembled ZnO nanodot with a single-crystalline structure showing hexagonal atomic arrays.

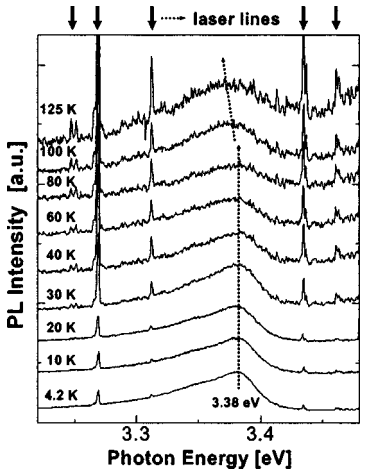

FIG. 13. Temperature-dependent μ-PL spectra of 100 nanodots in the ZnO-nanodot sample presented at Fig. 2(a).

As a consequence, Zn and O species supplied during MOCVD growth for ZnO rods are concentrated beneath the precipitates. The FE-SEM image of Fig. 3(c) shows that only a small number of ZnO rods appeared to grow perpendicular to the surface of the nanohole. Moreover, the lengths of the rods are much shorter than those of the rods inclined from the surface normal, which serves as additional evidence for a catalyst-poisoning effect.

D. Low-dimensional quantum characteristics of selective grown ZnO nanodots

We previously reported on quantum confinement effects from self-assembled ZnO nanodots by MOCVD on SiO_2/Si substrates.[1] However, since the spatial distribution of the nanodots fabricated by self-assembly is still random, it is difficult to achieve desirable characteristics for ZnO nanostructure-based devices. In this regard, the realization of low-dimensional ZnO nanodots well manipulated in size and positions is strongly desirable. The μ-PL measurements were performed to confirm low-dimensional quantum characteristics of the selectively grown ZnO nanodots. The temperature-dependent PL measurements were carried out from 4.2 to 300 K in a cryostat. Approximately 100 nanodots with a uniform size [shown in Fig. 2(a)] arranged in the diameter (7.5 μm) of the focused laser spot were excited.

The μ-PL spectra are presented in Fig. 13. At 4.2 K, the main peak position of the spectrum with a broad full width at half maximum (FWHM) of about 80 meV is around 3.380 eV. Usually, a free-exciton emission (EX) from ZnO thin films on SiO_2/Si, Si, and Al_2O_3 is located at about 3.377 eV at low temperature (10 K),[1,20,21] and the energy position of the near-band-edge (NBE) emission is barely related to the crystal structure of ZnO. It has been reported that the PL spectrum of amorphous ZnO films shows a strong ultraviolet emission (NBE emission).[22] Therefore, it is reasonable to conclude that the emission from 100 nanodots in this study is

shifted to the higher-energy side. Moreover, the emission energy was independent of temperature below 80 K. Sharp peaks that were not shifted with temperature originated from the emission of the He–Cd laser, which is frequently observed when the intensity of the PL emission from a sample is weak and which is a good reference for calibrating PL energy.

First, the cause of the observed blueshift is discussed. There are two possible explanations: one is the quantum size effects from the nanodots,[1,23] and the other is band-gap widening by the Burstein–Moss (BM) effect[24] which could occur due to the unintentional doping effect of Ga atoms into the nanodots during MOCVD growth. Calculations were performed concerning the quantum effect. The infinite potential barrier was introduced to clarify the band-gap enhancement by the quantum size effect in the ZnO nanodots. The average height and average width of nanodots are 9 and 130 nm, respectively, as mentioned in Sec. III B, indicating that the dimension of the dots is much larger than the excitonic ZnO Bohr radius of 1.8 nm. In this case, the center-of-mass motion of excitons is quantized by the confinement potential and the relative carrier motion is dominated by the Coulomb interactions. This is the so-called weak confinement.[25] Assuming the Coulomb potential to be a small perturbation, the confinement energies were calculated by a combination of the Kronig–Penny model adopting "a particle in a box" and the Kayanuma model,[26] including the Coulomb potential. The band-gap enhancement was estimated from the shift in the EX band. The energy E of the EX band from the ZnO nanodots can be given by

$$E = E_{\mathrm{EX.ZnO}} + \frac{\pi^2\eta^2}{2}\left(\frac{1}{m_e^*}+\frac{1}{m_h^*}\right)\left[\left(\frac{n_x}{L_x}\right)^2+\left(\frac{n_y}{L_y}\right)^2 + \left(\frac{n_z}{L_z}\right)^2\right] - \frac{1.789e^2}{\varepsilon}\sqrt{\left(\frac{n_x}{L_x}\right)^2+\left(\frac{n_y}{L_y}\right)^2+\left(\frac{n_z}{L_z}\right)^2} - 0.248E_{\mathrm{Ryd}}, \quad (1)$$

where the exciton binding energy of 60 meV in bulk ZnO (the Rydberg value, E_{Ryd}) was employed and introduced into the Kayanuma model. The effective masses of electrons and holes are $m_e^*=0.24m_0$ and $m_h^*=0.45m_0$, respectively.[27] The average dot dimension derived from AFM measurement, $L_x=L_y=130$ nm and $L_z=9$ nm, is substituted into the Eq. (1). In addition, the third term can be neglected due to the fact that its calculated value is very small. Since the dot structures in this study are not capped, half of the dot surfaces are under stress-free conditions. From this fact, the strain-induced band-gap shift was not taken into account. Thus, the Eq. (1) can be simply expressed as

$$E = E_{\mathrm{EX,ZnO}} + C\left(\frac{n_x^2+n_y^2}{130^2}+\frac{n_z^2}{9^2}\right) - 0.014\,88\ \mathrm{eV}. \quad (2)$$

Here, $E_{\mathrm{EX,ZnO}}$ (energy position of the EX band in ZnO thin films) and C (the calculated confinement parameter) are 3.377 and 2.40 eV, respectively. The calculated EX energy at the lowest excited level ($n_x=n_y=n_z=1$) is 3.392 eV, which agrees well with the experimental PL results shown in Fig. 13. Another possible explanation for the blueshift, that is, the BM shift is discussed later.

Concerning broad linewidth (80 meV at 4.2 K), size distribution within the laser spot (7.5 μm) does not seem responsible because only 100 nanodots were excited. Since the ZnO nanodots in this work have nonburied structures and the emissions from them are only observed below 175 K, we speculate that the broad emission is related to the generation of nonradiative recombination centers at the surface of the ZnO nanodots. In addition, the asymmetry of the spectral shape with a long tail toward the lower-energy side of the spectrum might be interpreted as being due to the generation of surface defect levels.[28]

The anomalous PL temperature dependence mentioned in Fig. 13 can be mainly attributed to the thermal excitation of carriers among discrete energy levels.[29] The width of the nanodots in this study was as large as 130 nm, resulting in quantum-well-like 2D quantum confinement. In this situation, the energy gap between each level is very small, resulting in the easy excitation of a carrier from lower-energy to higher-energy levels by thermal energy. From the calculation of energy levels in the conduction band near the band gap of the ZnO nanodots using Eq. (2), the findings show that there are five discrete energy levels within 2 meV from the lowest excitation-energy level, showing that the band-gap shrinkage by thermal energy (estimated by Varshni equation[30] to be 6.7 meV up to 80 K, which is the temperature upper limit for showing no peak shift) can be compensated by the thermal excitation of carriers in the conduction band. Regretfully, we were not able to obtain more information from other samples with smaller dot dimensions [shown in Figs. 2(b) and 2(c)] due to the very weak emission at this stage.

The higher-energy shift of the PL spectra in Fig. 13 can be explained by the BM shift as another possibility, considering the possible unintentional Ga doping into the nanodots. The Fermi level in the conduction band of the degenerate semiconductor leads to a widening of the energy band, which is related to carrier concentration, n, by

$$\Delta E = \frac{h^2}{8m^*}\left(\frac{3n}{\pi}\right)^{2/3}. \quad (3)$$

The electron effective mass is expressed as m^*. Generally, however, the experimental results for the band-gap shift versus the carrier concentration do not exactly follow Eq. (3). Experimental results reported from some ZnO research groups have shown various exponent values ($2/3$, $1/3$, and $3/5$)[31–33] for Eq. (3). In heavily doped polar ZnO, the band-gap shift cannot be simply explained by only a BM shift because the widening of the band gap caused by the BM shift competes with the narrowing of the band gap by Coulomb interactions among the charged carriers and their scattering against ionized impurities.

Assuming that the BM shift is also observed at low temperature (4.2 K), we estimated the carrier concentration in the nanodots using the energy shift of the main peak observed in the μ-PL measurement at 4.2 K (Fig. 13) compared with the main peak position of a reference sample. The reference sample was a ZnO thin film on a SiO_2/Si substrate, used in our previous report.[1] The main peak position of the

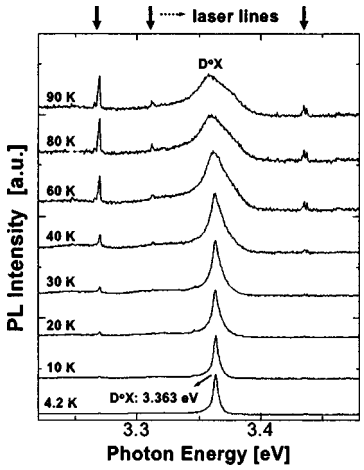

FIG. 14. Luminescence spectra obtained by temperature-dependent μ-PL measurements, using the same PL configuration introduced in Fig. 13, of selectively grown 100 nanodots with the dimension (average width and height is 170 and 20 nm, respectively).

D^0X emission from the reference sample is 3.366 eV, while the main peak position from the 100 ZnO nanodots in the μ-PL measurement at 4 K is 3.380 eV. In order to achieve this energy blueshift of 14 meV (=3.380−3.366 eV) only by a BM shift, the carrier concentration estimated from the Eq. (3) should be 6.23×10^{18} cm^{-3}, which looks a possible doping concentration. However, we did not observe a blueshift in the μ-PL measurements of selectively grown amorphous 100 nanodots with a larger dimension [average width and height (AFM results) is 170 and 20 nm, respectively] compared with the nanodots used in Fig. 13, as shown in Fig. 14. Moreover, the neutral donor-bound exciton (D^0X) emission located at 3.363 eV is sharp at 4.2 K and the peak shift toward a lower-energy side with temperature increase is clearly observed, which is very similar to the optical behavior of ZnO thin films. The fact that a blueshift was not observed in μ-PL measurements of nanodots with larger dimensions, in spite of the same FIB-patterned substrate (namely, the same doing concentration of Ga atoms), indicates that the blueshift is less related to the BM shift. In addition, regarding the temperature-dependent PL result shown in Fig. 13, the peak position of the main peak is hardly shifted up to the measurement temperature of 80 K. This result clearly shows that the contribution of the BM shift to the band-gap widening is insignificant because the band gap of a sample with a high carrier concentration generally shrinks with increasing temperature more drastically than that with a low carrier concentration.[34] Thus, we can conclude that the blueshift of the PL spectra from the nanodots is mainly due to low-dimensional quantum confinement in the ZnO nanodots.

IV. SUMMARY

The preparation of highly ordered ZnO-nanodot arrays with the periodicities of 750, 190, and 100 nm on FIB-manipulated SiO_2/Si substrates is described. A systematic study was performed, using TEM measurements to clarify the structural properties of the selectively grown ZnO nanodots. The findings indicate that the artificially assembled ZnO nanodots have amorphous structural properties and that Ga atoms, incorporated during the FIB engraving, play an important role in the artificial control of ZnO nanodots. The supply of Zn and O species results in the formation of amorphous ZnO nanodots on a surface that is supersaturated with respect to a Zn–Ga solid solution in the Ga-incorporated area into the FIB-patterned nanohole. An increase in MOCVD-growth time permitted nanodots to be changed into clusters and rods. The lengths of the rods perpendicular to the nanohole surface are much shorter than those of the rods inclined from the surface normal, which clearly demonstrates the catalyst-poisoning effect. Finally, from μ-PL measurements, we confirmed that the blueshift in the PL spectrum measured at the low temperature of 4.2 K from ZnO-nanodot arrays can be mainly attributed to the low-dimensional quantum characteristics of the ZnO nanodots.

ACKNOWLEDGMENTS

This work was partly supported by a grant-in-aid for scientific research and also by grants for regional science and technology promotion from the Ministry of Education, Culture, Sports, Science, and Technology of Japan.

[1] S.-W. Kim, Sz. Fujita, and Sg. Fujita, Appl. Phys. Lett. **81**, 5036 (2002).
[2] M. H. Huang *et al.*, Science **292**, 1897 (2001).
[3] W. I. Park, D. H. Kim, S.-W. Jung, and G.-C. Yi, Appl. Phys. Lett. **80**, 4232 (2002).
[4] Z. W. Pan, Z. R. Dai, and Z. L. Wang, Science **291**, 1947 (2001).
[5] J. J. Wu, S. C. Liu, C. T. Wu, K. H. Chen, and L. C. Chen, Appl. Phys. Lett. **81**, 1312 (2002).
[6] K. Hummer, Phys. Status Solidi B **56**, 249 (1973).
[7] S.-W. Kim, T. Kotani, M. Ueda, Sz. Fujita, and Sg. Fujita, Appl. Phys. Lett. **83**, 3593 (2003).
[8] X. D. Wang, C. J. Summers, and Z. L. Wang, Nano Lett. **4**, 423 (2004).
[9] S.-W. Kim, M. Ueda, T. Kotani, Sz. Fujita, and Sg. Fujita, Jpn. J. Appl. Phys., Part 2 **42**, L568 (2003).
[10] T. Aign *et al.*, Phys. Rev. Lett. **81**, 5656 (1998).
[11] M. M. Alkaisi, R. J. Blaikie, S. J. McNab, R. Cheung, and D. R. S. Cumming, Appl. Phys. Lett. **75**, 3560 (1999).
[12] A. Kumar, H. A. Biebuyck, and G. M. Whitesides, Langmuir **10**, 1498 (1994).
[13] M. Ueda, S.-W. Kim, Sz. Fujita, and Sg. Fujita, Jpn. J. Appl. Phys., Part 2 **43**, L652 (2004).
[14] S.-W. Kim, Sz. Fujita, and Sg. Fujita, Jpn. J. Appl. Phys., Part 2 **41**, L543 (2002).
[15] G. Benassayag, C. Vieu, J. Gierak, P. Sudraud, and A. Corbin, J. Vac. Sci. Technol. B **11**, 2420 (1993).
[16] X. Wang, Y. Ding, C. J. Summers, and Z. L. Wang, J. Phys. Chem. B **108**, 8773 (2004).
[17] Y. Li, W. Kim, Y. Zhang, M. Rolandi, D. Wang, and H. Dai, J. Phys. Chem. B **105**, 11424 (2001).
[18] B. D. Yao, Y. F. Chan, and N. Wang, Appl. Phys. Lett. **81**, 757 (2002).
[19] J. Zhong, S. Muthukumar, Y. Chen, Y. Lu, H. M. Ng, W. Jiang, and E. L. Garfunkel, Appl. Phys. Lett. **83**, 3401 (2003).
[20] K. Ogata, S.-W. Kim, Sz. Fujita, and Sg. Fujita, J. Cryst. Growth **240**, 112 (2002).
[21] H.-J. Ko, Y. F. Chen, Z. Zhu, T. Yao, I. Kobayashi, and H. Uchiki, Appl. Phys. Lett. **76**, 1905 (2000).
[22] Z. J. Wang, H. M. Zhang, Z. J. Wang, L. G. Zhang, and J. S. Yuan, J. Mater. Res. **18**, 151 (2003).
[23] K.-K. Kim, N. Koguchi, Y.-W. Ok, T.-Y. Seong, and S.-J. Park, Appl. Phys. Lett. **84**, 3810 (2004).
[24] E. Burstein, Phys. Rev. **93**, 632 (1954).
[25] U. Woggon, *Optical Properties of Semiconductor Quantum Dots*, Springer Tracks in Modern Physics, Vol. 136 (Springer, Berlin 1996).
[26] Y. Kayanuma, Phys. Rev. B **38**, 9797 (1988).
[27] E. M. Wong and P. C. Searson, Appl. Phys. Lett. **74**, 2939 (1999).
[28] E. Hanamura, J. Phys. Soc. Jpn. **28**, 120 (1970).

[29]C. Y. Liu, S. Yuan, J. R. Dong, S. J. Chua, M. C. Y. Chan, and S. Z. Wang, J. Appl. Phys. **94**, 2962 (2003).
[30]E. Y. P. Varshni, Physica (Amsterdam) **34**, 149 (1967).
[31]N. Malkomes, M. Vergohl, and B. Szyszka, J. Vac. Sci. Technol. A **19**, 414 (2001).
[32]A. P. Roth, J. B. Webb, and D. F. Williams, Phys. Rev. B **25**, 7836 (1982).
[33]B. H. Choi and H. B. Im, Thin Solid Films **193/194**, 712 (1990).
[34]H. Teisseyre, P. Perlin, T. Suski, I. Grzegory, S. Porowski, J. Jun, A. Pietraszko, and T. D. Moustakas, J. Appl. Phys. **76**, 2429 (1994).